NANO · MICRO small
www.small-journal.com

Dual Circularly Polarized Luminescence (CPL) and Piezoelectric Responses in Self-Assembled Chiral Nanostructures Derived from a Dipeptide Based Piezorganogel

*Umesh, Sayan Bera, and Santanu Bhattacharya**

Next-generation medical and consumer electrical devices require soft, flexible materials. Piezoelectric materials, capable of converting mechanical stress into electrical energy, are of interest across various fields. Chiral nanostructures, with inherent chirality, have emerged as potential piezoelectric materials. Peptide-based materials, known for self-assembly and stimuli responsiveness, hold promise for the utilization of chiral nanostructures. When combined with luminescent chromophores, peptides can generate aggregation-induced chiroptical effects like Circularly Polarized Luminescence (CPL) and Circular Dichroism (CD). In this study, a chiral organogel, L,L-1 is synthesized, and its self-assembly, mechanical properties, and chiroptical features are examined. The organogel exhibits thermo-reversible and thixotropic behavior, forming fibrillar networks and 2D-sheets upon cooling. CD spectroscopy reveals aggregation-induced chirality on pyrene chromophore, resulting in CPL with g_{lum} values of 3.0 ($\pm$ 0.2) $\times$ 10^{-3} and 3.1 ($\pm$ 0.2) $\times$ 10^{-3} for L,L-1 and D,D-1, respectively. Notably, the 2D-sheets exhibit an enhanced piezoelectric response (d_{33} $\approx$76.0 pm V^{-1}) compared to the fibrillar network (d_{33} $\approx$64.1 pm V^{-1}). Introducing an electron-deficient molecule into the solution forms a Charge-transfer (CT) complex, modulating the piezoelectric response to d_{33} $\approx$52.44 pm V^{-1}. This study offers a promising approach to optoelectronics design, presenting a chiral system with both CPL and piezoelectric responses, opening new possibilities for innovative applications.

1. Introduction

There is an unmet need for innovation of soft and flexible biocompatible materials that enable energy harvesting. Accordingly, there is a growing interest in piezoelectric materials due to their remarkable ability to convert mechanical stress into electrical energy and vice versa. When these materials are subjected to mechanical pressure, they generate an electric charge, and when an electric field is applied, they undergo mechanical deformation. This unique property is a result of the asymmetric distribution of positive and negative charges within the crystal lattice structure of such materials.[1–3] Piezoelectric materials possess several important characteristics and advantages that make them highly valuable in various biomedical applications, including actuation, tissue repair, bone defect repair, cardiac pacemakers, and bio-sensing etc.[4–8]

In addition to the conventional piezoelectric materials such as PVDF,[9,10] PVDF-TrFE, PAN, PVDF-PAN,[11,12] chiral nanostructures have attracted considerable attention owing to their inherent chirality and unique properties. Chiral nanostructures lack an inversion center, resulting in a net electric polarization even without an external electric field. When subjected to mechanical stress, these nanostructures experience a displacement of charges within their lattice, generating an electric potential and exhibiting the piezoelectric effect.[13–15] Peptide-based materials have emerged as promising candidates for chiral nanostructures due to their innate chirality, biocompatibility, and self-assembling capabilities. The noncovalent interactions, such as

Umesh, S. Bera, S. Bhattacharya
School of Applied and Interdisciplinary Sciences
Indian Association for the Cultivation of Science
Kolkata 700032, India
E-mail: sb@iisc.ac.in

S. Bhattacharya
Department of Organic Chemistry
Indian Institute of Science
Bangalore 560012, India

S. Bhattacharya
Technical Research Centre
Indian Association for the Cultivation of Science
Kolkata 700032, India

S. Bhattacharya
Department of Chemistry
Indian Institute of Science Education and Research
Tirupati 517619, India

The ORCID identification number(s) for the author(s) of this article can be found under https://doi.org/10.1002/smll.202308104

DOI: 10.1002/smll.202308104

hydrogen bonding, π–π stacking, and hydrophobic interactions, play a crucial role in organizing supramolecular nanostructures from peptides.[16] These interactions lead to the formation of various nanostructures, including gels,[17] micelles, vesicles, fibrillar networks, sheets, and tubes.[18–20] The weak nature of these non-covalent interactions allows these nanostructures to exhibit stimuli-responsive behavior in the presence of different external stimuli, such as changes in pH, temperature, redox conditions,[21] and light.[22–24]

Further, peptides, when tagged with luminescent moieties, may give rise to aggregation-induced chiroptical properties. Through the self-assembly process, the originally achiral organic chromophore acquires induced chirality, leading to unique chiroptical properties, including CPL, CD, etc.[25,26] CPL has garnered considerable recent attention due to its wide-ranging applications in optical information storage, 3D display encryption, and optical sensors. However, piezoelectricity and CPL are not directly related to each other in terms of their underlying principles or mechanisms. They are separate phenomena arising from different properties of materials. Materials possessing both CPL and piezoelectric responses manifest diverse applications in the fields of sensing, optoelectronics, and biomedical engineering. However, since reported instances of such materials are only a handful, the current focus of research in this area is on the development of new luminescent soft materials that possess dual CPL and piezoelectric properties which may play a significant role in sensing and biomedical engineering. For instance, the CPL can be used to detect and analyze the chiral purity of biomolecules, which is important in identifying specific target molecules, such as chiral drugs or biomarkers in clinical samples. CPL can enhance the selectivity of biosensors by providing information about the chirality of the detected molecules whereas the piezoelectric properties of materials can be employed in sensors to transduce the binding events between the target biomolecules and recognition elements (e.g., antibodies or aptamers) into measurable electrical signals. When the target molecules bind to the recognition elements on the sensor surface, it often induces a mechanical deformation, which can be detected as a change in the piezoelectric signal. By combining these two properties, the biosensor can thus provide highly selective detection of chiral biomolecules and amplify the detection signal through the piezoelectric effect.[27–30]

In response to the above objectives, we have synthesized the molecule L,L-1, featuring a dipeptide of well-defined stereochemistry at the Phe-core. The N-end is conjugated with a tri-3, 4, 5-(n-dodecyloxy) benzoic acid, while the C-end has a pyrenyl unit. Remarkably, L,L-1 forms an organogel in toluene, allowing us to thoroughly investigate its mechanical properties through rheological characterizations. Our study delved into the self-assembly of L,L-1 using various spectroscopic techniques, which revealed the formation of a fibrillar network upon microscopic investigations. Interestingly, upon cooling the solution to 10 °C, we observed the formation of 2D sheets, a finding which could be further ascertained spectroscopically.

The self-assembly of L,L-1 exhibited thermo-reversible and thixotropic characteristics, adding to its intriguing properties. Through CD spectral studies, we shed light on the aggregation-induced chirality exhibited by the originally achiral pyrene chromophore. This led us to explore the chiroptical properties of L,L-1, where we observed a positive CPL signal for L,L-1 and a negative CPL signal for D,D-1, with glum values of 3.0 ($\pm$0.2) $\times$ 10^{-3} and 3.1 ($\pm$0.2) $\times$ 10^{-3}, respectively. Notably, the 2D sheets showed no CPL presumably due to the lower emission intensity of pyrene. Additionally, our Piezo Force Microscopy (PFM) experiments demonstrated the piezoelectric response of L,L-1 presumably due to the presence of the dipolar nature of the amide bonds, directional H-bonding, and aromatic interactions. Modulating the electronic properties of pyrene allowed us to control the piezoelectric coefficient (d_{33}). For the fibrillar network, we observed d_{33} value of 64.1 pm V^{-1}, while after the formation of 2D sheets at lower temperatures, d_{33} increased to 76.0 pm V^{-1}. Furthermore, we introduced an electron-deficient 2,4,7-trinitrofluorenone (TNF) into a solution of L,L-1 (6 mM) in toluene, leading to the formation of a Charge-Transfer (CT) complex with the donor pyrene moiety. This was confirmed by the observation of a color change from the colorless of the solution to red and through various spectroscopic techniques, the charge transfer properties were examined. Interestingly, after the CT formation, we observed a decrease in the piezoelectric response, with a d_{33} value of 52.44 pm V^{-1}.

Thus, our findings represent a new and promising approach in the design and fabrication of soft materials, as the chiral system that exhibits both CPL and piezoelectric responses. We believe this exciting discovery could open up new avenues for innovative approaches in optoelectronic research.

2. Results and Discussion

The molecules L,L-1, and D,D-1 were synthesized with a dipeptide (Phe-Phe) core, N-protected with tri-3,4,5-(n-dodecyloxy) benzoic acid, and C-protected with an aminomethyl pyrene unit, following the methods described in the materials and methods section. Here "L" refers to the molecule derived from L-phenylalanine, while "D" indicates the molecule derived from D-phenylalanine. The final synthesized compounds were characterized extensively using ^{1}H-NMR, ^{13}C-NMR, FT-IR, and ToF-SIMS mass spectroscopy as shown in Figures S9–12 (Supporting Information), and the data were consistent with their given structures. To study the gelation capability of L,L-1, and D,D-1 in toluene, the typical heating–cooling method was employed, as depicted in **Figure 1**a. The results showed the formation of a self-supporting homogenous organogel in toluene by the gelators. The critical gelation concentration (CGC) for both the L,L-1, and D,D-1 in toluene was found to be ≈3.4 mM. However, when a 1:1 (racemic) mixture was used in toluene, no gelation was observed, underscoring the significance of chirality in the gelation behavior of these molecules. The microscopic images obtained from AFM, TEM, and FE-SEM (Figure 1b) displayed entangled fibrillar nanostructures of the xerogel.

2.1. Investigation of Self-Assembly Behavior

To further understand the material's behavior, rheological experiments were conducted to undertake detailed viscoelastic characterization.[27] The strain sweep rheological experiments were conducted at 25 °C with a constant oscillatory frequency of

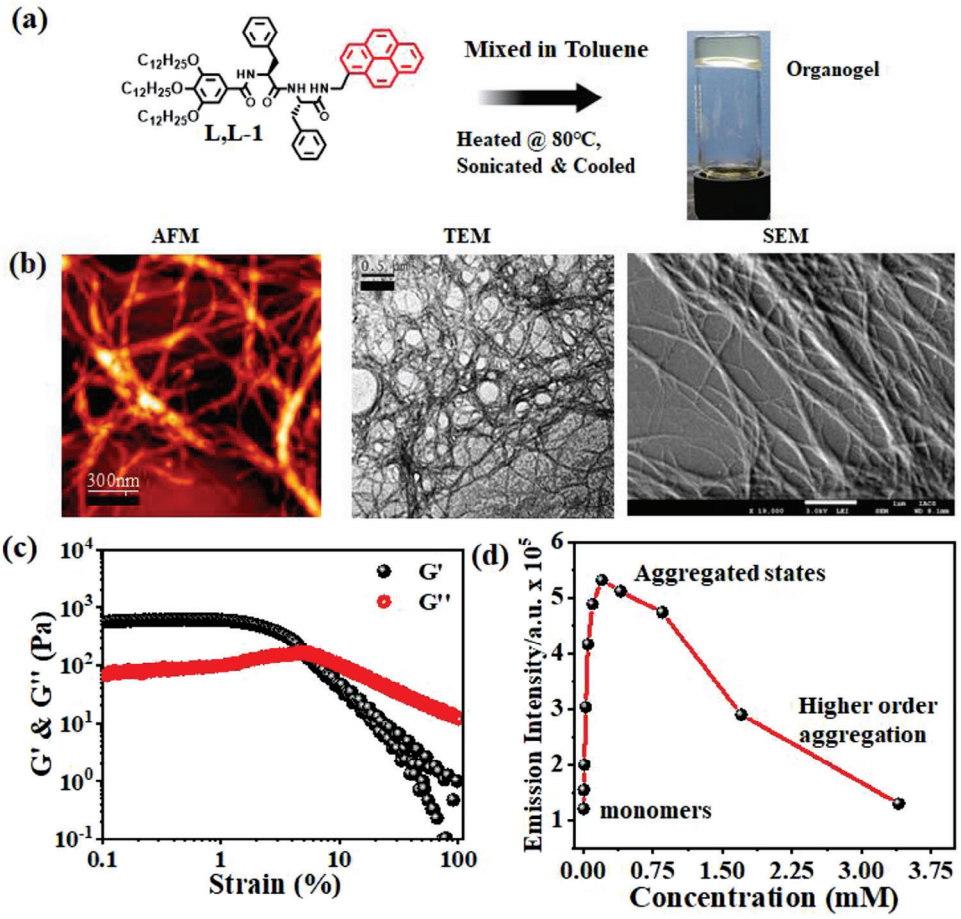

Figure 1. a) Molecular structure of the gelator and schematic illustration of the formation of organogel in toluene, b) AFM, TEM and SEM microscopic images of nanostructures formed by L,L-1 (0.5 mM) in toluene (Scale bar = 300 nm (AFM), 500 nm (TEM), and 1 μm (SEM)), c) variation of G' (solid black sphere) and G'' (hollow red circle) with oscillatory strain of L,L-1 organogel in toluene (6 mM) at 25 °C and angular frequency of 7 rad s^{-1}, and d) the plot of emission intensity of L,L-1 at 395 nm versus concentration.

7 rad s^{-1}, as shown in Figure 1c. The results revealed that the storage modulus (G'), associated with elastic contribution, was ≈6000 Pa, which exceeded the loss modulus (G'') of ≈600 Pa, representing the viscous behavior. This significant difference between G' and G'' indicated the solid-like behavior of the gel, with a critical strain value of ≈3% strain. Moreover, the high values of G' and G'' indicated a robust and firm gel structure. The gel exhibited a linear viscoelastic behavior across the entire frequency range studied (0.1–200 rad s^{-1}) in the oscillatory frequency sweep experiment, conducted at 25 °C with a constant strain of 0.1%, as shown in Figure S1a (Supporting Information). Notably, both G' and G'' showed no dependency on the oscillatory frequency, suggesting the gel's stability which are consistent with the mechanical properties manifested over this frequency range.

To investigate the thixotropic character of the gel, a hysteresis loop test was performed.[28,31,32] This involved applying successive higher strains (up to 100%) above the yield strain and lower strains (0.1%) within the linear viscoelastic region. The gel displayed a thixotropic behavior, as indicated by the hysteresis loop, with reversible changes in its structure upon the application and removal of higher strains. The results shown in Figure S1b (Supporting Information) demonstrate that upon applying a higher strain (100%), the gel undergoes a transition to the sol state, as evidenced from G' becoming less than G''. However, upon reducing the strain back to 0.1%, the gel quickly recovers its solid-like behavior, and remarkably, the values of G' and G'' return to their original pristine values, indicating the organogel's excellent thixotropic properties. This ability to reversibly shift between the gel and sol states makes the organogel a highly promising thixotropic material. Temperature sweep experiments were performed at a constant strain of 0.1% and an oscillatory frequency of 7 rad s^{-1} to investigate the thermal behavior of the organogel. The results in Figure S1c (Supporting Information) show a continuous decrease in both G' and G'' with increasing temperature, suggesting the gradual breakage of weak interactions involved in the nanostructure formation of the gel. Interestingly, there is a sudden increase in G'' (loss modulus) at 60 °C, indicating the gel-to-sol transition temperature (T_g) to be ≈60 °C. This critical temperature marks the point at which the gel structure weakens, leading to a transition from the solid-like gel state to the sol state.

To understand the phenomena better further, the self-assembly mechanism was thoroughly investigated through various physical methods, including UV–vis, fluorescence, and CD spectroscopy. The UV–vis spectra (depicted in Figure S2a,

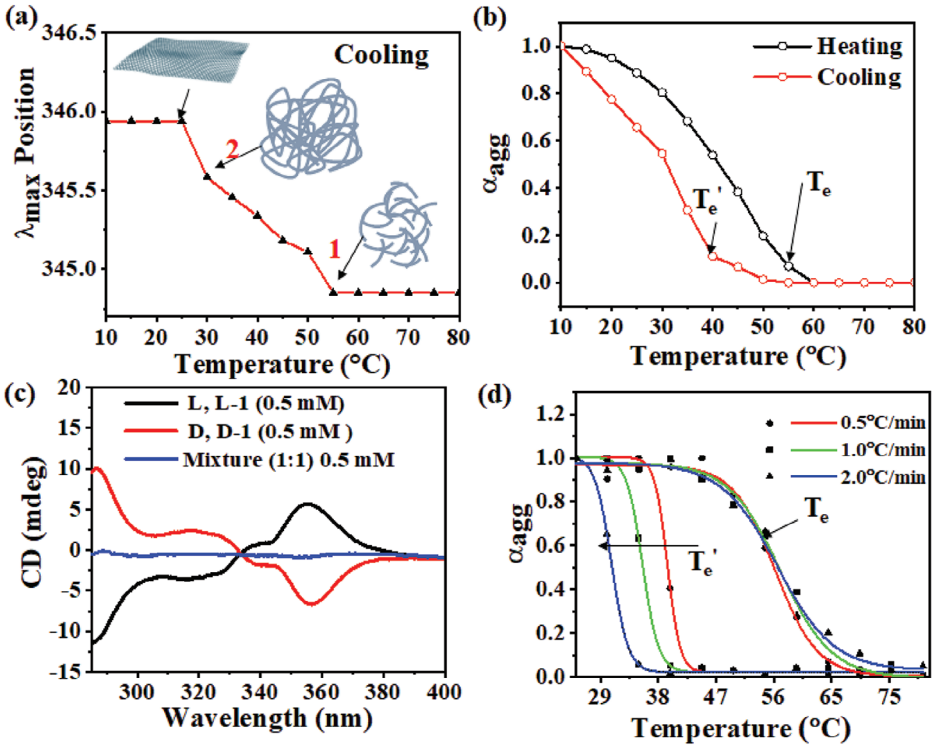

Figure 2. UV–vis absorption spectroscopy performed for the L,L-1 solution (0.5 mM) in toluene, a) the plot of λ_{max} position versus temperature upon cooling the L,L-1 solution, b) the plot of the temperature-dependent degree of aggregation (α_{agg}) of L,L-1 (0.5 mM, $\lambda = 345$ nm) versus temperature, CD spectroscopy performed for the L,L-1 solution (0.5 mM) in toluene, c) CD spectra of L,L-1 (0.5 mM), D,D-1 (0.5 mM), and equimolar mixture of both isomers recorded at 25 °C, and d) the plot of α_{agg} of L,L-1 (0.5 mM, $\lambda = 355$ nm) versus temperature recorded with varying heating/cooling rate from 0.5 to 2 °C min^{-1}.

Supporting Information) of L,L-1 revealed the presence of distinct absorption bands at 350, 330, 315, and 279 nm, corresponding to the π–π^*, n–π^* transitions attributed to the aromatic groups pyrene and phenylalanine, respectively.[33,34] Upon gradually increasing the concentration of L,L-1, a red-shifted absorption band emerges, spanning between 355 and 375 nm, accompanied by enhancements in the absorbance intensity of bands at 350, 330, and 315 nm. These observations strongly indicate the formation of aggregated states. Similarly, we investigated the concentration-dependent fluorescence spectra of L,L-1 to gain further insights. The findings presented in Figure S2b (Supporting Information) reveal the formation of an emission band centered at ≈400 nm for diluted solutions, which may be attributed to the monomeric form of the pyrenyl units. As the concentration of L,L-1 is increased, the emission intensity at 400 nm initially rises subsequently diminishes, and eventually vanishes. Notably, an emission band emerges, peaking at 425 nm with a shoulder at 465 nm, indicative of the presence of aggregated pyrenyl units.[35] The plot illustrating the relationship between the emission intensity at 395 nm and the concentration of L,L-1 (shown in Figure 1d) provides valuable insight, revealing a critical aggregation concentration (CAG) of 0.25 mM. The temperature-dependent fluorescence spectra of L,L-1 were also explored. As the temperature is increased (as shown in Figure S2c, Supporting Information), the intensity of the emission bands at 420 and 460 nm diminish, accompanied by the appearance of an emission band at 400 nm, signifying the transition from an aggregated to a monomeric state. Conversely, upon decreasing the temperature (as depicted in Figure S2d, Supporting Information), the intensity of the bands at 420 and 460 nm regains their initial levels, indicating the reformation of the aggregated states at lower temperatures.

To further delve into the self-assembly mechanism, temperature-dependent UV–vis spectroscopic measurements were conducted. Figure S3a (Supporting Information) displays the temperature-dependent absorption spectra of L,L-1 in toluene at a concentration of 0.5 mM. Cooling the solution from 80 to 10 °C at a rate of 1 °C min^{-1} leads to a red-shift of the absorption band at 345 nm, accompanied by reduced intensity. Additionally, a red-shifted shoulder appears in the ab-sorption range of 350–400 nm. This behavior is reversed upon heating the solution from 10 to 80 °C at the same rate (as shown in Figure S3b, Supporting Information), indicating the transition from the monomeric to the aggregated states of L,L-1. Furthermore, from the plot of λ_{max} position versus temperature (as depicted in **Figure 2**a), obtained upon cooling the 0.5 mM solution of L,L-1 in toluene, two distinct transitions are observed at temperatures of 55 and 30 °C. These thermotropic transitions signify the shift from monomeric to lower-order aggregated states and lower to higher-order aggregated states respectively. Additionally, the temperature dependent degree of aggregation (α_{agg}) was determined from the absorption at $\lambda = 345$ nm during the heating and cooling process.[35] The α_{agg} versus temperature plot (Figure 2b) exhibits a thermal hysteresis, with well-defined

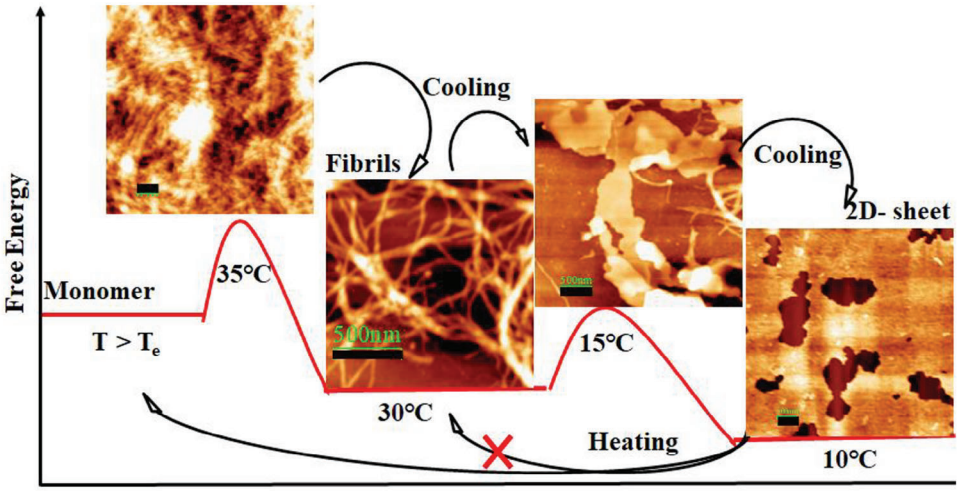

Figure 3. AFM microscopic images of L,L-1 (0.5 mM) at different temperature (35, 30, 15 and 10 °C) obtained by controlled cooling of the solution at a cooling rate of 1 °C min^{-1} and schematic depiction of structural transitions (Scale bar = 500 nm).

critical temperatures T_e (55 °C) and T_e' (40 °C) for heating and cooling, respectively. These critical temperatures underscore the influence of the heating-cooling rate on the self-assembly process of L,L-1.

To gain deeper insights into the abovementioned observations, CD spectral studies were undertaken. CD spectra were recorded for the solution of L,L-1 (0.5 mM) at 25 °C (as shown in Figure 2c), revealing a pronounced positive Cotton effect at 359 nm, accompanied by a negative band at 286 nm. These distinct CD bands signify the induction of chirality on the pyrenyl unit through the self-assembly. D,D-1 displayed CD bands that are enantiomeric mirror images of their L,L-1 isomers, while no CD signal was detected for the equimolar mixture of the two molecules. The temperature-dependent CD spectra of L,L-1 were then examined. Figure S3c (Supporting Information) illustrates the CD spectra of 0.5 mM L,L-1, acquired with a heating rate of 2 °C min^{-1}, as the temperature was raised from 10 to 80 °C. The intensity of the CD bands consistently diminishes as the temperature increases, eventually leading to no signal at higher temperatures. This trend suggests a transition from the aggregated to the monomeric state. Conversely, upon cooling with a cooling rate of 2 °C min^{-1} (as depicted in Figure S3d, Supporting Information), the intensity of the CD signal initially reaches a maximum at 25 °C and subsequently decreases progressively until reaching 10 °C. This observation aligns with the outcomes of the prior UV–vis studies in Figure 2a, further confirming the transition from monomeric to lower order aggregated states and then lower to higher order aggregated states.

The plot depicting the fraction of aggregated species (α_{agg}, λ = 355 nm) versus temperature (as shown in Figure 2d) was obtained from the CD absorption of the 0.5 mM L,L-1 solution in toluene. This plot provides additional insight into the temperature-dependent behavior of the self-assembly process, highlighting the dynamic nature of the aggregation states.[35–37] The observed sigmoidal transitions suggest the involvement of an isodesmic mechanism in the self-assembly process of L,L-1. Notably, a thermal hysteresis was evident during the heating and cooling processes, with distinct critical temperatures T_e for heating and T_e' for cooling. Interestingly, the value of T_e' shifted to lower temperatures as the cooling rate was increased from 0.5 to 2 °C min^{-1} within the temperature range of 80–25 °C. This observation suggests that the self-assembly process is under kinetic control and does not follow rapid temperature changes. Conversely, the value of T_e was not affected by the change in the heating rate, indicating that the disassembly process of L,L-1 is under thermodynamic control. Furthermore, the decrease in CD signal intensity observed upon cooling beyond 25 °C is attributed to the transition of the aggregated state.

2.2. Morphological Characterization

To investigate this transition of the aggregated states, atomic force microscopy (AFM) was employed. **Figure 3** illustrates that upon cooling the sample at a rate of 1 °C min^{-1}, fibrillar nanostructures were initially formed at 30 °C, which then underwent a structural reorganization and transformed into 2D-sheet-like structures at 10 °C. Moreover, the formation of fibrillar nanostructures was not observed upon heating the 2D-sheet nanostructures (Figure S5, Supporting Information). Time-variant CD spectroscopy was utilized to investigate the formation of fibrillar nanostructures.

The CD spectra in **Figure 4**a were recorded by cooling the solution of L,L-1 (0.5 mM) at a cooling rate of 1 °C min^{-1} to 30 °C, and then the CD signal at 355 nm was monitored as a function of time at 30 °C. No change in the CD signal intensity was observed for 15 min, indicating that the fibrillar structures are kinetically stable. However, the signal intensity decreases upon cooling the solution to 25 °C, suggesting that the fibrillar structures are only kinetically stable but not thermodynamically stable at this temperature.

2.3. Chiroptical Properties

Examination of CD spectra further revealed the chirality induction on the pyrenyl unit through self-assembly, providing

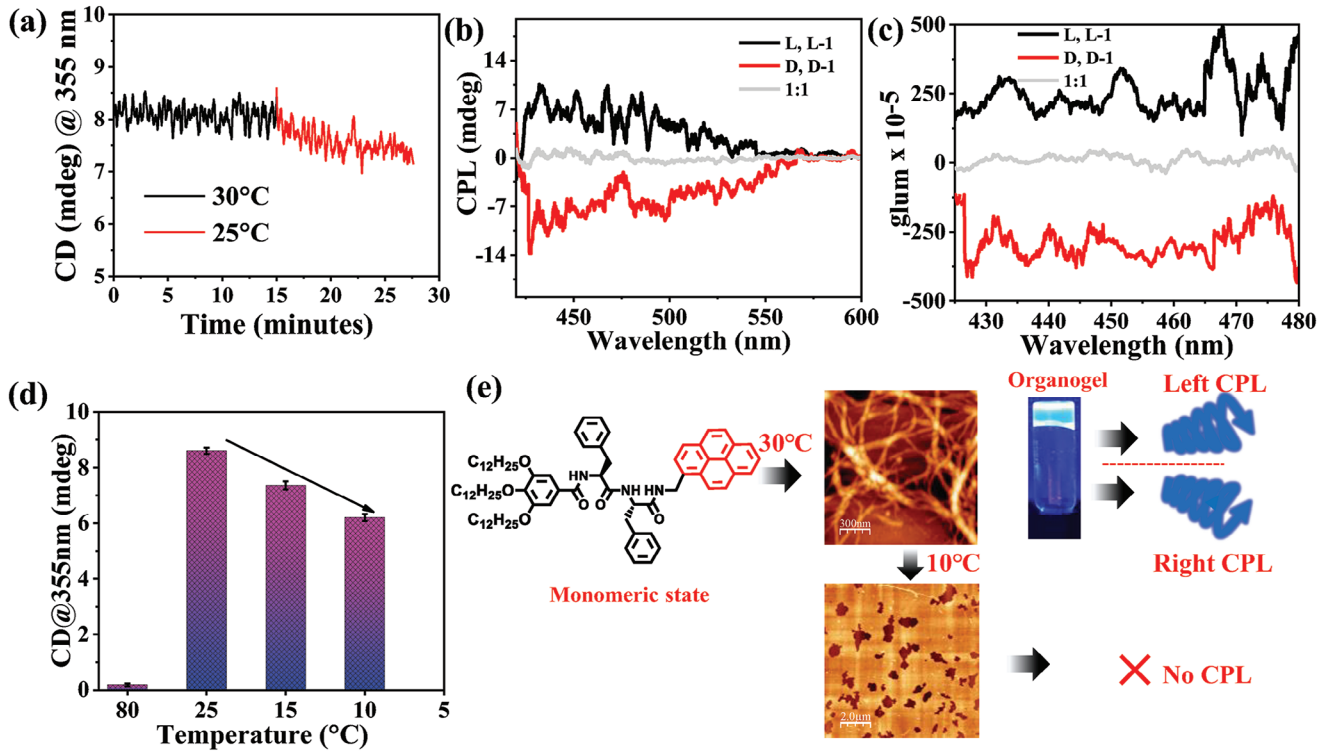

Figure 4. Chiroptical properties of the L,L-1, a) time variation CD spectra for L,L-1 solution (0.5 mM) at $\lambda = 355$ nm, b) CPL spectra of L,L-1 gel (black line) and D,D-1 gel (red line) excited at $\lambda_{exc} = 326$ nm, c) luminescence dissymmetry factor (g_{lum}) for the gels, d) CD@355 nm on cooling the L,L-1 solution, and e) schematic illustration of the induced CPL via the self-assembly of L,L-1/D,D-1.

valuable insights into the ground state of the chiral system. To further explore the excited state of the chiral system L,L-1/D,D-1, CPL spectroscopy was employed. The anisotropy factor (g_{lum}) was used to quantify the extent of chiral fluorescence dissymmetry,[38,39] given by the formula $g_{lum} = 2\,(I_L - I_R)/(I_L + I_R)$, where I_L and I_R represent the intensities of left and right circularly polarized light, respectively. The CPL signals originating from the self-assembly of the gelators are shown in Figure 4b. L,L-1 exhibited a positive Cotton effect, while D,D-1 displayed a negative Cotton effect at 25 °C when fibrillar nanostructures existed in the solution while no CPL signal was detected for the equimolar mixture and 2D sheets (Figure S6b, Supporting Information). However, upon cooling the solution to 10 °C, 2D sheets were formed, and the CPL signal diminished which could be attributed to the decrease in the CD absorption leading to the disruption of chiral stacking of the pyrene units shown in Figure 4d. Lower DC values observed for 2D sheets in the CPL measurement (Figure S6c, Supporting Information). The g_{lum} values observed for L,L-1 and D,D-1 were found to be 3.0 (±0.2) × 10^{-3} and 3.1 (±0.2) × 10^{-3}, respectively (Figure 4c). These values are in the same order as those reported for the physical organogels with other organic chromophores.[40,41]

2.4. Investigation of Charge Transfer Complex Formation

Further, the influence of a charge transfer complex on the self-assembly of L,L-1 was investigated. To achieve this, an electron acceptor, 2,4,7-trinitrofluorenone (TNF), was introduced into a toluene solution of L,L-1 in a 1:1 ratio, with pyrene serving as the donor. The formation of the charge transfer complex (CT complex) between L,L-1 and TNF was initially observed by the appearance of a red color in the solution, as depicted in **Figure 5**a. Subsequently, other spectroscopic techniques were employed to further probe the CT complexation. The UV–vis results displayed a distinct charge transfer band at ≈525 nm (Figure 5b), which provided concrete evidence for the presence of the CT complex. This was further substantiated by fluorescence spectroscopy, where the addition of electron-deficient TNF resulted in the quenching of pyrene emission (Figure 5c). The ^{1}H-NMR spectra in Figure 5d exhibited presence of broad NMR peaks of the pyrene proton in the $\delta = 7.95$–7.65 ppm region, indicating an aggregated state of the molecules. Additionally, an upfield shift was observed upon the addition of electron-deficient TNF to the solution, further confirming the formation of the CT complexes.

The investigation of the mechanical strength of the gel formed by the 1:1 (L,L-1:TNF) assembly through rheological experiments revealed valuable insights. Interestingly, no gelation was observed for the 1:2 (L,L-1:TNF) ratio. The strain sweep rheological experiments conducted at 25 °C with a constant oscillatory frequency of 7 rad s^{-1} (Figure 5e) demonstrated a critical strain value of ≈1.0%, which was lower than the L,L-1 gel with 3.0% strain. This suggested that the CT gel exhibited lower endurance toward strain. However, the magnitudes of G′ and G″ for the CT gel were found to be similar to the L,L-1 gel in the "LIVE" region,

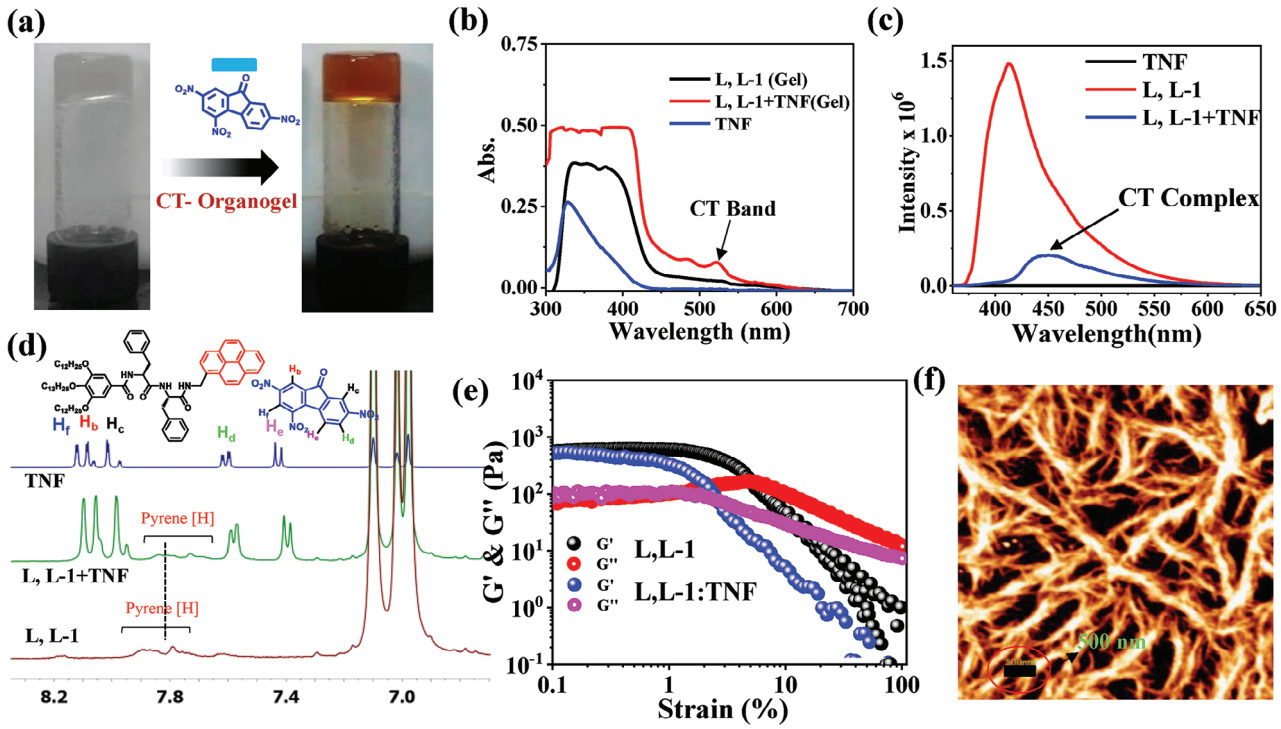

Figure 5. a) photos of organogel with (red) and without (colorless) CT complex, b) UV–vis spectra, c) fluorescence spectra, d) ^{1}H-NMR spectra of L,L-1: TNF, L,L-1, and TNF, e) variation of G' and G'' with oscillatory strain of L,L-1:TNF (1:1) organogel in toluene (6 mM) at 25 °C and angular frequency of 7 rad s^{-1}, and f) AFM image of L,L-1:TNF (1:1) organogel (Scale bar = 500 nm).

indicating comparable viscoelastic properties. Furthermore, the AFM image (Figure 5f; Figure S6d, Supporting Information) revealed the presence of a fibrillar network in the CT gel, which provided visual evidence for the gel's structural characteristics.

2.5. Piezoelectric Properties

Having examined the self-assembly mechanism of L,L-1 and the influence of pyrene on the process, particularly its temperature-dependent behavior and its modification due to the charge transfer (CT) complex formation, our next objective was to explore the piezoelectric response of the resulting chiral nanostructures. These nanostructures lack an inversion center, and when subjected to mechanical stress, they exhibit a phenomenon known as the piezoelectric effect, wherein a displacement of charges occurs, generating an electric potential. In this regard, we have performed the piezoresponse force microscopy (PFM). Accordingly, the samples were prepared on conducting ITO-coated glass substrates, and subsequent PFM measurements were done by monitoring the amplitude or phase response of the samples against an applied external bias. The relationship between the mechanical strain (deformation) experienced by the material and the resulting electrical charge generated is quantified by the piezoelectric coefficient (d_{33}). The piezoelectric coefficient can be expressed as: $d = e / S$, where: "d" is the piezoelectric co-efficient, "e" is the induced electric charge in response to applied mechanical stress, and "S" is the applied mechanical stress (measured as force per unit area).

At a temperature of 25 °C, the self-assembled fibrous network formed by L,L-1 demonstrated a remarkable piezoelectric response, exhibiting a distinctive amplitude loop opening commonly known as a "butterfly loop" as illustrated in **Figure 6**a. The fibrous network exhibited an observed piezoelectric coefficient (d_{33}) of ≈64.1 pm V^{-1}, stemming from the synergistic interplay of several factors, including the dipole moment of amide bonds, directional value of hydrogen bonding, and pyrene stacking within the chiral nanostructures.[15,42] Intriguingly, when investigating the 2D sheet nanostructures, an increase in the piezoelectric coefficient (d_{33}) to ≈75.9 pm V^{-1} was noted (Figure 6b). This enhancement in the piezoelectric response could be attributed to the presence of higher-ordered pyrene stacks within the 2D-sheet chiral nanostructures, signifying the significant influence of pyrene on the piezoelectric characteristics of the L,L-1 molecule. To gain a deeper understanding of the role of pyrene in the piezoelectric response, the fibrous nanostructures formed by the interactions of the CT complex were utilized (Figure 6c). Height, amplitude, and phase image acquired from PFM are shown in Figure S8 (Supporting Information). Surprisingly, a decrease in the magnitude of the piezoelectric coefficient (d_{33}) to ≈52.44 pm V^{-1} (Figure 6d) was observed for the CT complex-based fibrous nanostructures. This finding confirms that pyrene stacks indeed play a crucial role in enhancing the piezoelectric properties of the L,L-1 molecule.

3. Conclusions

In conclusion, in this work, we have successfully designed, synthesized, and developed chiral organogels, e.g., L,L-1 and D,D-1

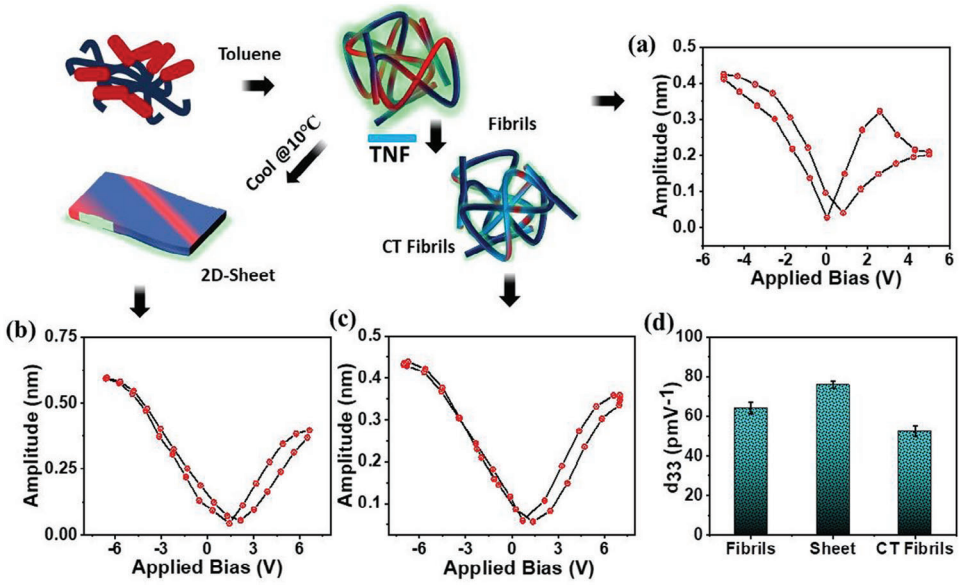

Figure 6. PFM amplitude loops acquired for the a) fibers formed by L, L-1 (0.5 mM) at 30 °C, b) 2D-sheets formed by L,L-1 (0.5 mM) at 10 °C, c) fibers formed by CT Complex of L,L-1: TNF (1:1, 0.5 mM), and d) variation of piezoelectric coefficient (d_{33}) with different nanostructures formed by L,L-1.

derived from L-phenylalanine- and D-phenylalanine-based moieties, respectively. These materials are soft and can hold liquids while maintaining well-defined yet deformable structures. The critical gelation concentration (CGC) in toluene was found to be ≈3.4 mM, and the organogels exhibited entangled fibrillar nanostructures, as characterized by AFM, TEM, and FE-SEM. Rheological experiments revealed the gel's robust and firm structure with solid-like behavior, and it displayed thixotropic properties, transitioning reversibly between the gel and sol states. Temperature sweep experiments indicated a gel-to-sol transition temperature (T_g) of ≈ 60 °C. Spectroscopic techniques, including UV–vis, fluorescence, and CD, provided valuable insights into the self-assembly mechanism, indicating the formation of aggregated states and the induction of chirality in the pyrenyl unit. CPL spectroscopy showed the chiral fluorescence dissymmetry in the self-assembled gel, and the piezoelectric response of the fibrous nanostructures was explored. The piezoelectric coefficient (d_{33}) was remarkably enhanced in the 2D-sheet nanostructures, suggesting the significant influence of pyrene on the piezoelectric characteristics of L,L-1. The results from this study highlight the fascinating properties and potential applications of chiral piezorganogels. The understanding of the self-assembly mechanism and the induction of chirality in the pyrenyl unit could inspire the design of novel chiral functional materials for various optoelectronic, sensing, and biomedical applications. Furthermore, the study also provides valuable insights into the structure-property relationships, offering the potential for rational design and tuning of gel properties. By exploring different di- or oligo-peptide cores and by modifying the protecting groups, it may be possible to tailor the mechanical strengths, chiroptical, piezoelectric responses, and other properties of the organogels to suit specific applications including design of biologically inspired highly flexible and stretchable systems. We believe that piezoelectric organogel based self-powered systems are extremely limited at the moment and may soon find use in diverse areas such as portable electronics, electronic skin, biomechanics, organ transplants, and even artificial intelligence. With a focused multidisciplinary effort in the search for hitherto unknown biopiezoelectric organo-/hydrogels and related self-assembled systems, we envisage improved prospects of making green energy and achieving appropriate biological applications. Work is underway to achieve such goals in our laboratory.

4. Experimental Section

Preparation of Gel: To prepare a gel, a weighed amount of dry gelator (5 mg) L,L/D,D-1 was transferred into a glass vial followed by addition of toluene (1 mL). The resulting mixture was heated at 80 °C and then bath-sonicated for 10 min to convert it into nearly clear solution. The solution was allowed to cool at room temperature for 30 min. The gelation was confirmed using the inversion of tube method. Each of the experiments was performed in duplicate. If a gel was formed, minimum gelator concentration (MGC) depicting the minimum amount of gelator required to immobilize 1 mL of a particular solvent was evaluated quantitatively.

Rheological Studies: Mechanical properties of the gel were examined by rheological experiments performed on Anton Paar MCR 302 Modular compact rheo-meter by using a cone plate on a Peltier plate. The diameter of the cone plate used for the experiments was 25 mm with cone angle 2 and the gap between plates was 115 µm.

Atomic Force Microscopy (AFM): The organogel was diluted to a concentration of 0.5 mm and drop casted on a freshly cleaved mica. Each sample was air-dried at room temperature and then analyzed by Asylum Research MFP-3D AFM in tapping mode.

Transmission Electron Microscopy (TEM): The diluted solution of organogel (10 µL) was drop-casted onto a carbon-coated copper grid (300 mesh size) and air-dried at room temperature. Samples were further stained with 0.1% uranyl acetate solution. TEM images of dried samples were then acquired at an accelerating voltage of 200 kV using a high-resolution JEOL JEM 2010 transmission electron microscope (HR-TEM).

Scanning Electron Microscopy (SEM): The diluted organogel was carefully drop-coated over cover slips which were then stuck onto brass stubs and were allowed to freeze-dry overnight. The samples were then coated with platinum vapors and analyzed on a JEOL JEM 6700F scanning electron microscope (SEM) operated at 5 kV.

UV–Vis Spectroscopy: The diluted solutions of organogel were used for the UV–vis spectroscopy experiments. All the UV–vis experiments were performed on a Shimadzu UV-2600 UV–vis spectrophotometer using a quartz cuvette with a 1 mm path length. For the temperature-dependent UV–vis spectroscopy of gel, a Julabo 300F model heating circulator was attached to Shimadzu UV-2600 UV–vis spectrophotometer to control the temperature of the sample. in a quartz cuvette with 1 mm path length kept in a holder from 20 to 70 °C. All the spectra were collected in the text file and used Origin 2018 to plot the final data.

The degree of aggregation (α_{agg}) refers to the extent to which individual molecules or particles come together to form larger structures or aggregates. It is a measure of how closely packed or clustered these entities are within a material or solution.

The degree of aggregation is calculated from the temperature-dependent UV–vis spectra by using the following equation:

$$\alpha\text{agg} = (A\text{u} - A\text{t})/(A\text{u} - A\text{a}) \quad (1)$$

where: i) A_t is the absorbance at a particular temperature; ii) A_u is the absorbance at the final temperature; and iii) A_a is the absorbance at the final lowest temperature.

Fluorescence Spectroscopy: Fluorescence spectra of the diluted organogel solutions were recorded on Fluoromax-4 model Spectrofluorometer using a quartz cuvette with 10 mm path length.

FT-IR Spectroscopy: The organogel was dried under vacuum and then powder xerogel was analyzed by Perkin Elmer Spectrum model 100 FT-IR system using calcium fluoride cell.

Circular Dichroism (CD) Spectra: CD spectra of the organogel were recorded by using a 1 mm quartz cuvette in a JASCO J-815 model spectrophotometer. Each of the CD spectra was the average of three scans, smoothed and zero corrected.

The degree of aggregation is calculated from the temperature-dependent circular dichroism measurements by using the following equation:

$$\alpha\text{agg} = (\theta\text{t} - \theta\text{u})/(\theta\text{a} - \theta\text{u}) \quad (2)$$

where: i) θ_t is the observed ellipticity value at a particular temperature; ii) θ_u is the ellipticity value at the final temperature; iii) θ_a is the ellipticity value at the final lowest temperature.

To calculate the critical temperatures T_e for heating and T_e' for cooling we plotted the fraction of aggregated species [α_{agg}, ($\lambda = 345$ nm, for UV), ($\lambda = 355$ nm, for CD)] against temperature and fitted with the mathematical model.

NMR Spectroscopy: ^{1}H and ^{13}C NMR spectra were recorded in FT-NMR Bruker DPX 500 MHz and operating at 125 MHz for ^{13}C NMR spectrometer. Chemical shifts were reported in ppm.

CPL Measurements: CPL spectra were recorded by using a 1 mm Quartz cuvette in a JASCO CPL-300 spectrophotometer with a double prism linearly polarizing monochromator to avoid linear polarization effects. Each spectrum was recorded with multiple spectral accumulations.

PFM Measurements: Piezoelectric force microscopy (PFM) experiments were done with an Asylum Research MFP-3D atomic force microscope (AFM) with a Ti/Ir (5/20) coated cantilever (ASYELEC-01, nominal spring constant of 2.0 N m^{-1}, and resonance frequency of 81 kHz). PFM phase, amplitude images, and plots at a bias voltage of ±4 V were recorded.

Time-of-Flight Secondary Ion Mass Spectrometry: TOF-SIMS experiments were performed using an ION-TOF TOF-SIMS 5–100 (ION-TOF GmbH, Münster, Germany) equipped with a Bi LMIG and a GCIB Ar electron impact source. A pulsed 30 keV Bi^{3+} analysis beam and a direct current 2.5 kV Ar_q^+ sputter beam was used for this study. Both beams struck the target at an angle of 45°. The Bi LMIG gun was used in a high current, high mass resolution (HMR) mode for spectral scanning and in fast imaging mode with delayed extraction in order to acquire the 2D images. To acquire secondary ion images, Bi_3^+ was typically rastered over a 200 × 200 μm^2 area, centered inside a 500 × 500 μm^2 Ar_q^+ crater. Target currents were measured separately before each measurement in the pulsed mode for Bi_3^+ and the direct current mode for Ar^{q+}. The Bi_3^+ current was 0.5 pA in the HMR mode (<0.7 ns pulse width), 0.06 pA in fast imaging mode (minimum beam diameter & lt; 120 nm @ 400 pA DC). The Ar_q^+ current was ≈0.7 nA. The Bi LMIG was operated at a frequency of 10 kHz. The mass resolutions (measured at $C_2H_3^+$, m/z 27^+) were typically >12 000 (HMR mode) and >5000 (fast imaging mode). Positive spectra produced from the Bi_3^+ primary ion beam were mass calibrated using CH_3^+, $C_2H_3^+$, $C_3H_5^+$, and $C_4H_7^+$. Low energy electrons were flooded onto the sample to compensate for charge buildup. The 2D images were collected in the "noninterlaced" mode, where the analysis and sputter beams are simultaneously active in different TOF-cycles. This operation mode was necessary to produce images with sufficient secondary ion intensities.

Supporting Information

Supporting Information is available from the Wiley Online Library or from the author.

Acknowledgements

Umesh and S.B. thank IACS, and CSIR for research fellowships, respectively. This work was supported by the J.C. Bose Fellowship (DST) awarded to S.B.

Conflict of Interest

The authors declare no conflict of interest.

Author Contributions

The manuscript was written through the contribution of all authors. All authors had given approval to the final version of the manuscript. Umesh as the first author of the manuscript uploaded the final version of the manuscript after due verification of all the data and figures as obtained upon experiments.

Data Availability Statement

The data that support the findings of this study are available in the supplementary material of this article.

Keywords

chirality, circularly polarized luminescence (CPL), organogel, peptide, piezoelectric

Received: September 15, 2023
Revised: October 17, 2023
Published online:

[1] M. C. Sekhar, E. Veena, N. S. Kumar, K. C. B. Naidu, A. Mallikarjuna, D. B. Basha, *Cryst. Res. Technol.* **2023**, *58*, 2200130.
[2] Q. Kou, B. Yang, H. Lei, S. Yang, Z. Zhang, L. Liu, H. Xie, Y. Sun, Y. Chang, F. Li, *ACS Appl. Mater. Interfaces* **2023**, *15*, 37706.
[3] Y. Wang, S. Liu, L. Li, H. Li, Y. Yin, S. Rencus-Lazar, S. Guerin, W. Ouyang, D. Thompson, R. Yang, K. Cai, E. Gazit, W. Ji, *J. Am. Chem. Soc.* **2023**, *145*, 15331.

[4] A. Sharma, V. Panwar, B. Mondal, D. Prasher, M. K. Bera, J. Thomas, A. Kumar, N. Kamboj, D. Mandal, D. Ghosh, *Nano Energy* **2022**, *99*, 107419.
[5] A. Babu, V. Gupta, D. Mandal, *Appl. Phys. Lett.* **2022**, 120.
[6] S. Chibh, N. Aggarwal, Z. Mallick, D. Sengupta, P. K. Sachdeva, C. Bera, N. Yadav, V. S. Chauhan, D. Mandal, J. J. Panda, *Biomater. Sci.* **2023**, *11*, 3469.
[7] G. Li, Z. Li, Y. Min, S. Chen, R. Han, Z. Zhao, *Small* **2023**, *19*, 2302927.
[8] D. W. Jin, Y. J. Ko, C. W. Ahn, S. Hur, T. K. Lee, D. G. Jeong, M. Lee, C.-Y. Kang, J. H. Jung, *Small* **2021**, *17*, 2007289.
[9] F. Mokhtari, B. Azimi, M. Salehi, S. Hashemikia, S. Danti, *J. Mech. Behav. Biomed. Mater.* **2021**, *122*, 104669.
[10] T.-M. Guo, Y.-J. Gong, Z.-G. Li, Y.-M. Liu, W. Li, Z.-Y. Li, X.-H. Bu, *Small* **2022**, *18*, 2103829.
[11] S. Mohammadpourfazeli, S. Arash, A. Ansari, S. Yang, K. Mallick, R. Bagherzadeh, *RSC Adv.* **2023**, *13*, 370.
[12] Y. Zeng, L. Jiang, Q. He, R. Wodnicki, Y. Yang, Y. Chen, Q. Zhou, *J. Phy. D: Appl. Phy.* **2021**, *55*, 013002.
[13] D. Yang, R. Zhang, S. Gai, P. Yang, *Mater. Horiz.* **2023**, *10*, 1140.
[14] J. Harden, N. Diorio, A. G. Petrov, A. Jakli, *Phys Rev E* **2009**, *79*, 011701.
[15] S. Paul, S. Barman, A. Pal, A. Mukherjee, S. Ghosh, A. Datta, *Chem. Mater.* **2023**, *35*, 6463.
[16] T. Vijayakanth, B. Xue, S. Guerin, S. Rencus-Lazar, N. Fridman, D. Thompson, Y. Cao, E. Gazit, *J. Mater. Chem. C* **2023**, *11*, 5174.
[17] S. Datta, S. Bhattacharya, *Chem. Soc. Rev.* **2015**, *44*, 5596.
[18] I. W. Hamley, *Soft Matter* **2011**, *7*, 4122.
[19] A. Dehsorkhi, V. Castelletto, I. W. Hamley, *J. Pept. Sci.* **2014**, *20*, 453.
[20] K. Kumar, P. Moitra, M. Bashir, P. Kondaiah, S. Bhattacharya, *Nanoscale* **2020**, *12*, 1067.
[21] S. Bhunia, A. Peña-Duarte, H. Li, H. Li, M. F. Sanad, P. Saha, M. A. Addicoat, K. Sasaki, T. A. Strom, M. J. Yacamán, C. R. Cabrera, R. Seshadri, S. Bhattacharya, J.-L. Brédas, L. Echegoyen, *ACS Nano* **2023**, *17*, 3492.
[22] B. Maiti, S. Bhattacharjee, S. Bhattacharya, *Nanoscale* **2019**, *11*, 2223.
[23] P. Moitra, K. Kumar, P. Kondaiah, S. Bhattacharya, *Angew. Chem., Int. Ed.* **2014**, *53*, 1113.
[24] P. Moitra, Y. Subramanian, S. Bhattacharya, *J Phys Chem B* **2017**, *121*, 815.
[25] Q. Li, J. Zhang, Y. Wang, G. Zhang, W. Qi, S. You, R. Su, Z. He, *Nano Lett.* **2021**, *21*, 6406.
[26] J. Roose, B. Z. Tang, K. S. Wong, *Small* **2016**, *12*, 6495.
[27] Y. Sang, J. Han, T. Zhao, P. Duan, M. Liu, *Adv. Mater.* **2020**, *32*, 1900110.
[28] D. Niu, L. Ji, G. Ouyang, M. Liu, *Chem. Commun.* **2018**, *54*, 1137.
[29] B. Wu, H. Wu, Y. Gong, A. Li, X. Jia, L. Zhu, *J. Mater. Chem. C* **2021**, *9*, 4275.
[30] J. Liang, N. Zhang, X. Hu, A. Hao, P. Xing, *J. Mater. Chem. C* **2020**, *8*, 4321.
[31] Umesh, S. Sarkar, S. Bera, P. Moitra, S. Bhattacharya, *Mater Today Chem* **2023**, *30*, 101554.
[32] A. Garzón, A. Navarro, D. López, J. Perles, E. M. García-Frutos, *J. Phys. Chem. C* **2017**, *121*, 27071.
[33] F. Würthner, T. E. Kaiser, C. R. Saha-Möller, *Angew. Chem., Int. Ed.* **2011**, *50*, 3376.
[34] X.-D. Xu, J. Zhang, X. Yu, L.-J. Chen, D.-X. Wang, T. Yi, F. Li, H.-B. Yang, *Chem. - Eur. J.* **2012**, *18*, 16000.
[35] Z. Gao, S. Qiu, F. Yan, S. Zhang, F. Wang, W. Tian, *Chem. Sci.* **2021**, *12*, 10041.
[36] S. Ogi, V. Stepanenko, K. Sugiyasu, M. Takeuchi, F. Würthner, *J. Am. Chem. Soc.* **2015**, *137*, 3300.
[37] G. Markiewicz, M. M. J. Smulders, A. R. Stefankiewicz, *Adv. Sci.* **2019**, *6*, 1900577.
[38] S. Sarkar, B. Narayan, S. J. George, *ChemNanoMat* **2020**, *6*, 1169.
[39] A. Das, S. Ghosh, S. J. George, *Angew. Chem.* **2023**, *60*, e202308281.
[40] Y. Ohishi, M. Inouye, *Tetrahedron Lett.* **2019**, *60*, 151232.
[41] Z. Cao, F. Zhu, A. Hao, P. Xing, *J. Phys. Chem. C* **2020**, *124*, 7965.
[42] D. Gupta, A. Bhatt, V. Gupta, C. Miglani, J. P. Joseph, J. Ralhan, D. Mandal, M. E. Ali, A. Pal, *Chem. Mater.* **2022**, *34*, 4456.